J Infrared Milli Terahz Waves (2016) 37:209–229
DOI 10.1007/s10762-015-0221-1

System Development and Performance Testing of a W-Band Gyrotron

Sung Gug Kim[1] · Ashwini Sawant[1] · Ingeun Lee[1] · Dongsung Kim[2] · MunSeok Choe[2] · Jong-Hyo Won[3] · Jungho Kim[3] · Joonho So[4] · Won Jang[4] · EunMi Choi[1,2]

Received: 8 June 2015 / Accepted: 29 October 2015 /
Published online: 14 November 2015

Abstract A high-power W-band gyrotron has been designed and performance tested in Korea, with an output power in the range of tens of kilowatts. The gyrotron consists of a diode-type electron gun operating at 40 kV, a TE6,2 mode interaction cavity, and a mode converter for producing a highly Gaussian output mode beam. Presented here are the detailed component design procedure and the experimental results of the gyrotron's performance evaluation. A maximum power of 62 kW was achieved with an efficiency of 22 %, and a highly Gaussian output beam was observed. The gyrotron's output beam is analyzed, and its transmission through an oversized waveguide is discussed. This gyrotron is the first gyrotron developed in Korea with high power greater than 10 kW and high frequency greater than 90 GHz.

Keywords Gyrotron · Millimeter wave · High-power sources

1 Introduction

Gyrotrons are high-power, high-frequency devices that offer promise for several suitable applications including plasma heating, material processing, and biomedical imaging [1–3]. One urgently needed gyrotron application is fusion-related plasma heating in the International

✉ EunMi Choi
emchoi@unist.ac.kr

[1] School of Electrical and Computer Engineering, Ulsan National Institute of Science and Technology (UNIST), Ulsan 689-798, Republic of Korea

[2] Physics Department, Ulsan National Institute of Science and Technology (UNIST), Ulsan 689-798, Republic of Korea

[3] LIG Nex1, Pankyo, Republic of Korea

[4] Agency for Defense Development (ADD), Daejeon 305-152, Republic of Korea

Table 1 Design parameters of the gyrotron

Design parameters	Values
Frequency	W-band
Beam voltage	40 kV
Beam current	7.0 A
Cavity B-field	3.56 T
Axial distance from the emitter to the cavity	30.5 cm
Velocity ratio	1.3
Perpendicular velocity spread	<5 %
Magnetic compression ratio	23
Current density	<3 A/cm^2

Thermonuclear Experiment Reactor (ITER), which requires a 170-GHz gyrotron with output power of 1 MW for electron cyclotron heating (ECH) of ITER plasmas. To achieve this goal, a global effort has been undertaken by Japan, Russia, and the European Union [4, 5]. For this application, gyrotron developers have indeed pushed the highest available power limit to the MW level, with even a 2-MW unit proposed by employing a coaxial structure [6–8]. The gyrotron community has worked hard to resolve the technical obstacles that must be overcome, and these technical limitations have promoted innovations that may impact other science and engineering disciplines. In addition, active researchers have been investigating high-frequency gyrotrons, approaching 1 THz, filling the gap in the range between millimeter wavelengths and the infrared region (IR). A terahertz gyrotron has been exposed for its unchallenged high-output power capability even in the terahertz range, unlike other solid state-based sources [9–12]. The terahertz gyrotron offers potential for applications spanning from nondestructive detection in security to biomedical applications such as dynamic nuclear polarization (DNP)-nuclear magnetic resonance (NMR), which have been suggested and realized [13–15]. The terahertz gyrotron's capability for enhancing the current sensitivity of NMR is an especially promising application, and many universities, research institutions, and commercial companies are devoting resources to develop this capability [16–18]. In addition to the MW gyrotron, those with a medium range of output power, in the tens of kilowatts, and with high frequencies, greater than 30 GHz, have applications that include ceramic sintering, material processing, security scanning systems, and high-resolution millimeter-wavelength radar [19, 20]. Furthermore, new and interesting ideas, such as the use of a medium power gyrotron for advanced drilling technology as suggested by Woskov et al., have been proposed recently [21]. In this application, the

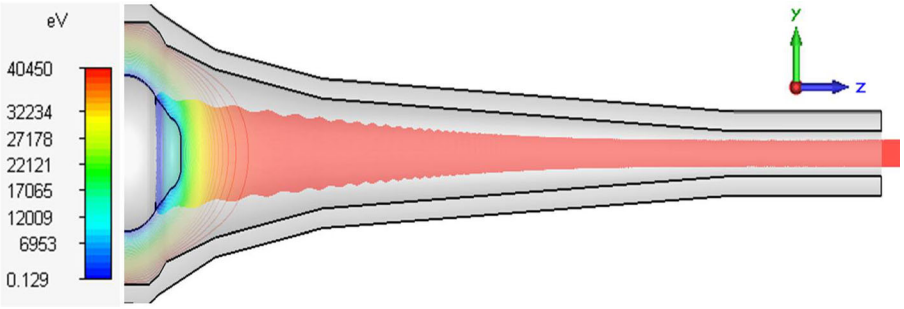

Fig. 1 Beam trajectory result from the CST PS for the diode-type magnetron injection gun (MIG)

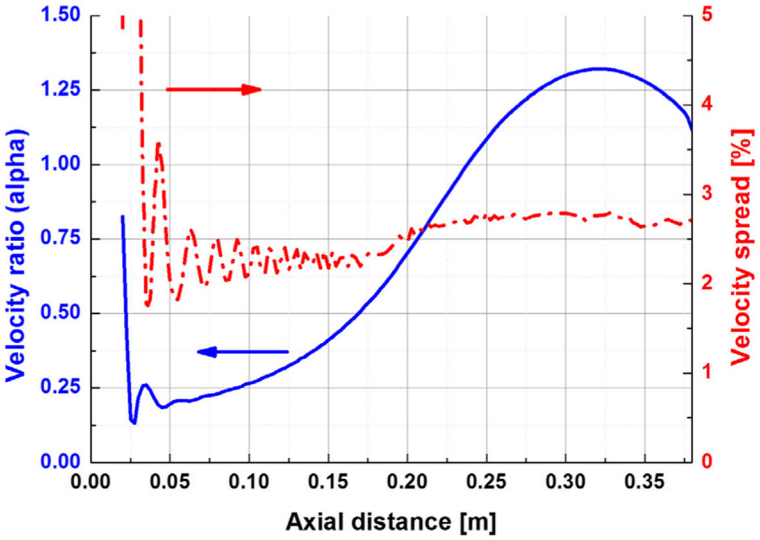

Fig. 2 Velocity ratio and velocity spread as a function of the travelling axis

researchers demonstrated that granite, basalt, and limestone can be melted and vaporized at temperatures over 3000 °C in a few minutes using a 28 GHz, 10 kW gyrotron [22, 23]. The Karlsruhe Institute of Technology (KIT) group also proposed a possible commercial use for the gyrotron to achieve uniform heat treatment on ceramics in a specially designed hexagonal chamber [24]. Lastly, the gyrotron's potential application in high-resolution millimeter-wavelength radar has become of worldwide interest in the development of high technology equipment to support advanced security capability.

In this study, we propose the development of a W-band gyrotron with an output power of approximately 30 kW for possible applications such as material processing and high-resolution radar systems, and possibly to extend to additional industrial applications. This work represents the first development effort in Korea in the high-frequency range with high-output power greater than 10 kW. The following sections present a detailed design of the gyrotron's critical components, as well as experimental results from its performance evaluation. The full system, including beam coupling to an oversized waveguide, is presented.

2 Gyrotron System Design and Cold Test

In this section, the designs for several important circuit components and their test results in the absence of an electron beam (cold test) are discussed in detail, including the gyrotron's electron gun, cavity, mode converter, window, and transmission line.

Table 2 Beam parameters summary of the MIG

Code	Guiding center radius	Velocity ratio	Velocity spread	Compression ratio
EGUN code	2.8133	1.317	3.198	22.443
CST PS	2.8175	1.267	4.673	22.443

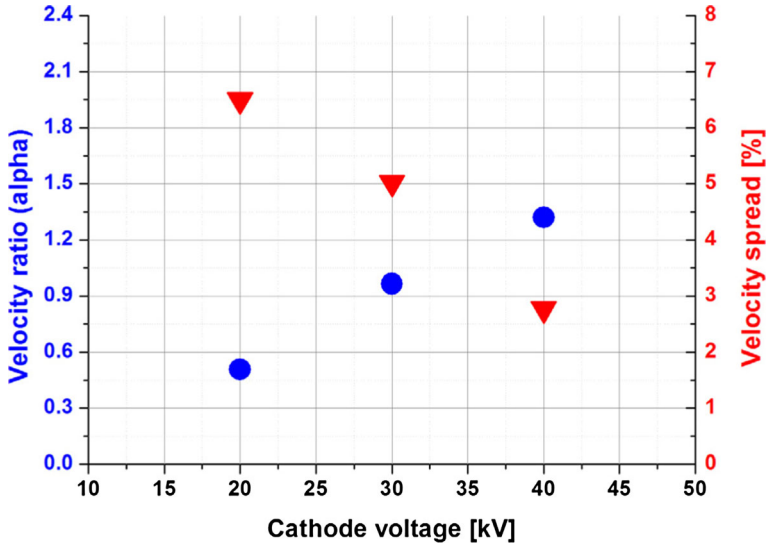

Fig. 3 Velocity ratio and velocity spread results as a function of cathode voltage obtained by the EGUN simulation

2.1 Electron Gun

A diode-type magnetron injection gun (MIG) was chosen as the gyrotron's electron gun. The design parameters for the electron gun are summarized in Table 1. Two numerical codes, the two-dimensional EGUN and the three-dimensional CST Particle Studio (CST PS), were used to design and optimize the electron gun geometry. The magnetic field that guides the electron beam was produced by a solenoid coil whose flattop is 10 mm at 3.56 T. An auxiliary gun coil (maximum field of 0.1 T) was added in the gun side to control beam radius and velocity ratio. The result from the CST PS is shown in Fig. 1, in which the full transmission of the electron beam is verified and visualized. Figure 2 shows the velocity ratio and the velocity spread due to electron ray optics as a function of the travelling axis obtained by the EGUN code.

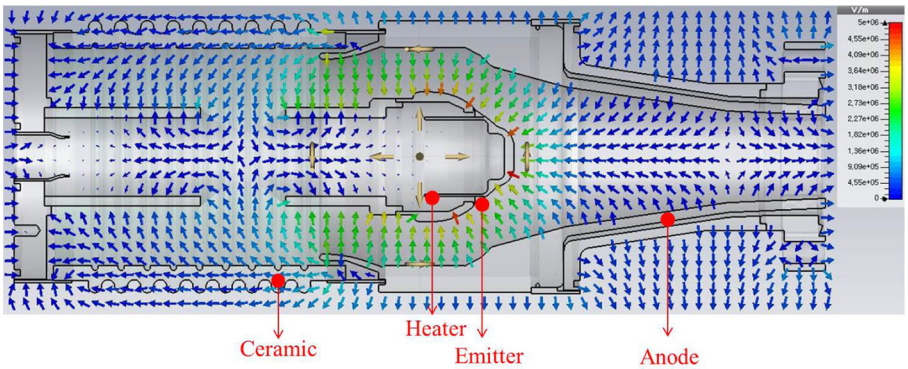

Fig. 4 Electric field analysis: *gray areas* represent metal and the *green area* is the insulator. The *color gradient of the arrows* represents the electric field strength

Table 3 Summary of thermal analysis of MIG

Material		Cathode	Emitter	Anode
Molybdenum	Temperature (°C)	830~1010	1010	36
	Deformation (mm)	0.07	0.16	0.0017
Stainless Steel	Temperature (°C)	830~1010	1010	62
	Deformation (mm)	0.07	0.16	0.018
Copper	Temperature (°C)	830~1010	1010	32
	Deformation (mm)	0.07	0.16	0.005

Figure 2 demonstrates that the velocity ratio reaches the designed value, and the velocity spread condenses at less than 5 %. Beam parameters obtained from two different simulation codes are summarized in Table 2. The results from the two codes agree reasonably well, although some discrepancy in the velocity ratio is observed.

In Fig. 3, the velocity ratio and velocity spread obtained by the EGUN simulation are plotted as a function of cathode voltage. Figure 4 shows the electric field strengths of the electron gun. The geometry was further optimized such that no electrical breakdown occurred. To minimize the electric field intensity, we rounded rough corners and secured sufficient space between the anode and the cathode stalk. A corona shield was added in the region between the cathode stalk and insulator where the highest electric field appeared. The final maximum electric field intensity was 74 kV/cm in a vacuum condition of approximately 10^{-9} Torr, which is below the breakdown threshold of the electric field.

After optimization of the MIG design, thermal analysis of the structure was carefully conducted using ANSYS software. For the temperature-dependent deformation analysis of each component, the steady state thermal solver and static structure solver of ANSYS software have been used. The initial temperatures of all components as well as the heat exchange coefficients between each material, heat flow, radiation, and convection boundaries are also set and applied. The maximum temperatures and thermal deformation of the cathode, emitter, and anode in different material types are summarized in Table 3. Figure 5 shows the temperature variations throughout the

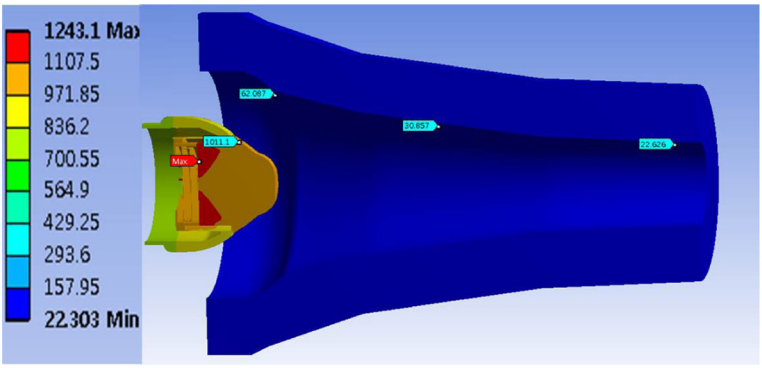

Fig. 5 Thermal analysis result from the ANSYS code for the stainless steel material

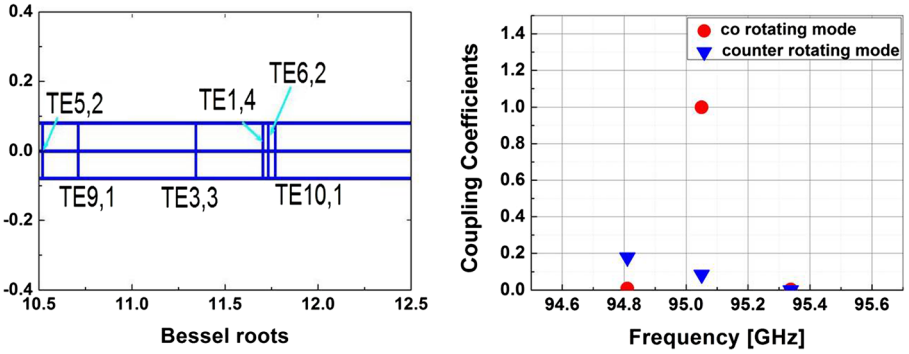

Fig. 6 Competition modes and the result of the coupling coefficients

geometry for the stainless steel case. The structural deformation due to increased temperature is within an allowable tolerance.

2.2 Interaction Cavity

A conventional-type cavity consisting of tapers at both ends was selected for our medium power W-band gyrotron. The diameter of the interaction cavity D (mm) was chosen such that the desired operating mode could be excited inside the cavity, which can be expressed as

$$D = 300\frac{\nu'_{mp}}{\pi f} \tag{1}$$

where ν'_{mp} is the pth root of the derivative of the Bessel function, J'_m, and f is the operating frequency in gigahertz.

A TE6,2 mode was selected as an operating mode for the target frequency. Neighboring modes that could compete with the TE6,2 mode were identified and plotted, as shown in Fig. 6. The corotating TE6,2 mode exhibited the maximum coupling to the electron beam at the desired beam radius that could enable a sole excitation in the cavity. The starting current as a function of the magnetic field and voltage was simulated and is shown in Fig. 7.

The TE6,2 mode was not seen to suffer from mode competition with other neighboring modes and would therefore indicate the stable operation of the gyrotron.

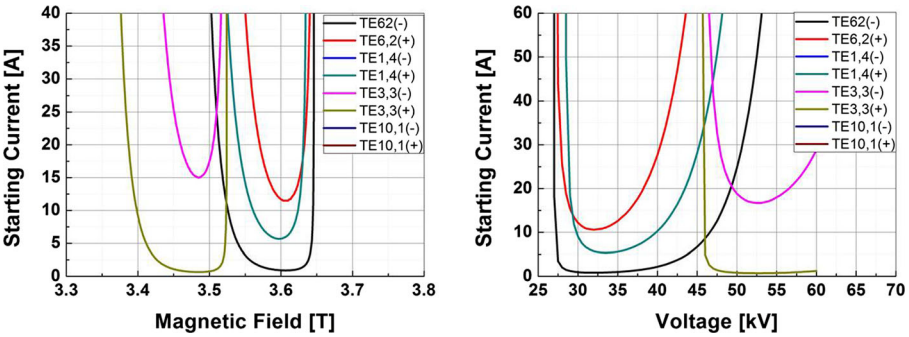

Fig. 7 Starting current as a function of the magnetic field and voltage

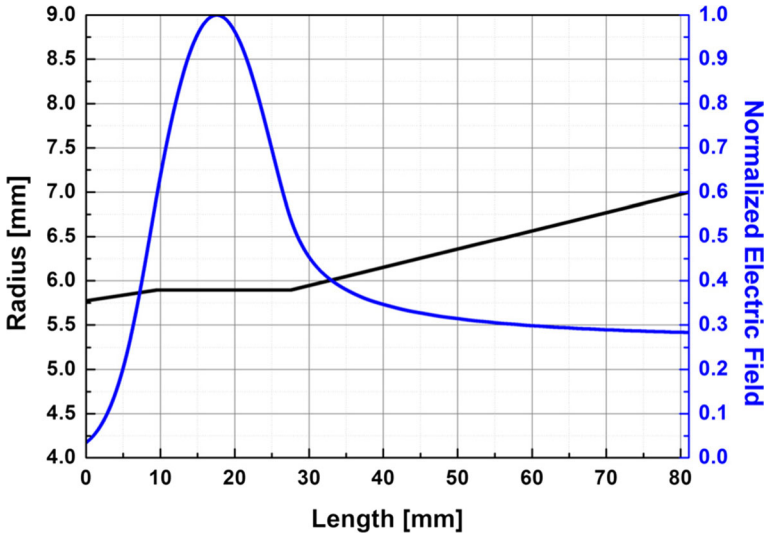

Fig. 8 Cavity profile and normalized electric field profile along the cavity length

The geometry of the cavity is shown in Fig. 8, and its geometrical parameters are detailed in Table 4. A simulation of the gyrotron cavity was conducted by a recent, internally developed code, the UNIST Gyrotron Design Tool (UGDT) version 1.0, and a commercially available three-dimensional particle-in-cell MAGIC code. The internally developed UGDT version 1.0 code was used to identify the oscillation frequency and quality factor of the gyrotron cavity by solving a second-order homogeneous Vlasov equation for electromagnetic field using Numerov's method and a single mode approximation [25, 26]. The result of this cold test simulation of the gyrotron cavity is shown in Fig. 8, illustrating both the cavity geometry and the normalized electric field profile. The resonant frequency and the quality factor of the cavity were determined to meet the condition of minimum reflection at the output end. The resonant frequency and quality factor obtained were 95.15 GHz and 904, respectively. The simulation results of this cold test of the cavity were confirmed experimentally with a nondestructive method in our previous study [27].

The UGDT version 1.0 is a one-dimensional, self-consistent, multimode code that simultaneously solves the electron motion equation using the predictor-corrector method and the radio frequency (RF) field equation using the leapfrog integration method for minimum reflection. A simulation of the hot-test (in the presence of an electron beam) of the cavity was also performed by

Table 4 Geometrical parameters of the gyrotron cavity

Design parameters	Values
Input radius (mm)	5.773
Cavity radius (mm)	5.895
Output radius (mm)	7.0
Input taper length (mm)	9.551
Cavity length (mm)	18
Output taper length (mm)	53.549

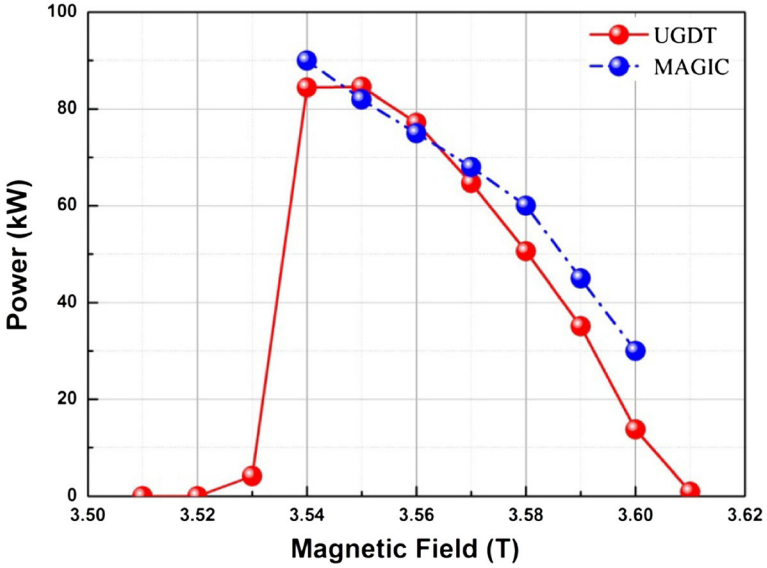

Fig. 9 Results of output power relative to variations in the magnetic field

UGDT and compared to MAGIC. The simulation results obtained from MAGIC and UGDT are shown in Fig. 9, and they are in good agreement. These simulations were conducted by neglecting the velocity spread and voltage depression. The computational time of the MAGIC code is extremely long compared to that of the UGDT simulation; the MAGIC requires approximately 5 days with approximately 1,023,120 mesh cells (mesh size of 0.2 mm × 0.2 mm × 0.5°), whereas the UGDT requires only 5 min and 10,000 mesh cells with a longitudinal mesh size of 0.81 μm. The maximum simulated output powers in MAGIC and UGDT are 90 and 82 kW, respectively, in a magnetic field of 3.54 T with a cathode voltage of 40 kV and a beam current of 7 A, with a maximum efficiency of 32 and 29 %, respectively, as shown in Fig. 9.

2.3 Quasi-Optical Mode Converter

In this section, we introduce the design of an internal quasi-optical mode converter (QOMC).

The QOMC was designed using a commercially available Surf3d code and LOT (Lexam Research) [28]. The designed QOMC is composed of a dimpled-wall helical cut launcher (DHCL) whose design parameters are summarized in Table 5 and four mirrors. The DHCL is located after the open-ended cavity and concurrent with the beginning of the internal QOMC [29]. The focusing of the electric field produced by the DHCL wall perturbation is plotted in Fig. 10. As shown in Fig. 10, the TE6,2 mode is uniformly distributed in the azimuthal direction and is becoming a well-focused beam shape. As the beam passes through the DHCL, it diverges rapidly. Therefore, the first mirror was designed using a quasi-parabolic equation for beam convergence:

$$\begin{aligned} x &= 2f_p tan\left(\frac{\phi}{2}\right) + r_{caustic}\left[1 + \phi tan\left(\frac{\phi}{2}\right)\right] \\ y &= f_p\left[tan^2\left(\frac{\phi}{2}\right) - 1\right] + r_{caustic}\left[\frac{\phi}{2}tan^2\left(\frac{\phi}{2}\right) + tan\left(\frac{\phi}{2}\right) - \left(\frac{\phi}{2}\right)\right] \end{aligned} \tag{2}$$

Table 5 Design parameters of DHCL

Operating mode	TE6,2
Radius of the launcher	7 mm
Length of the launcher	65.4 mm
Cut length of the launcher ($L_{\text{axial cut}}$)	21.965 mm
Caustic radius (r_{custic})	3.579 mm
Brillouin angle (θ_B)	58.9973°
Azimuthal bounce angle (φ)	59.2498°
Focal length	14 mm

where $r_{caustic}$ is the caustic radius, and f_p and φ are the focal length of the parabolic mirror and the azimuthal bounce angle of the propagating beam, respectively. $r_{caustic}$ and φ are given by

$$r_{caustic} = \frac{m}{k_\perp} = r_{wg}\frac{m}{v'_{mp}} \tag{3}$$

$$\varphi = \arccos\left(\frac{m}{v'_{mp}}\right). \tag{4}$$

where $k_\perp$ is the transverse wave number of the beam, m is the azimuthal mode index, and r_{wg} and v'_{mp} are the radius of the cylindrical waveguide and the pth nonvanishing zero of the derivative of the Bessel function J'_m, respectively.

The profile equation for the rest of mirrors is given by

$$z = \sqrt{R_x^2 - x^2} + \sqrt{R_y^2 - y^2} - \left(R_x + R_y\right) \tag{5}$$

where R_x and R_y are the mirror curvature radius in x and y direction, respectively.

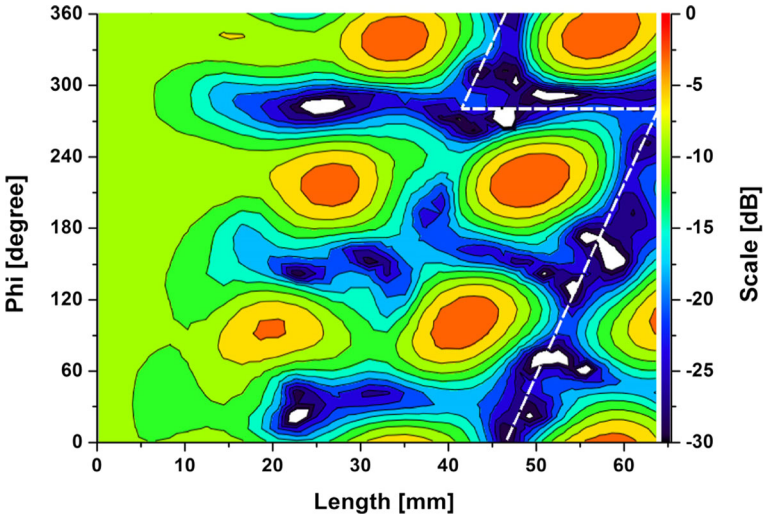

Fig. 10 Wall field intensity of the TE6,2 mode

Table 6 Design curvature parameters of mirrors

	M1	M2	M3	M4
R_x (cm)	2.8	9.73	500	20.0
R_y (cm)	Flat	9.73	500	15.5

A third flat mirror (M3) is included in the design because the beam reflected by M2 diffuses slowly. The reflected beam from the last mirror (M4) propagated out of the output window. Table 6 summarizes the detailed curvature parameters for each mirror.

Figure 11a shows the fabricated mirrors and DHCL, and Fig. 11b shows the QOMC assembly. To test the performance of the designed internal mode converter, a cold test of the QOMC was conducted experimentally by using a vector network analyzer (Agilent PNA-X5247A) with the OML WR08 extenders and with a rotating mode generator (RMG) [30]. The result of the mode converter test is shown in Fig. 12. The experimentally measured electric field intensity in each plane shows good agreement with the simulation. The performance of the mode converter can be quantified by comparing experimental results to simulation using a cross-correlation function (CCF), defined using both the amplitudes and phases and expressed as follows, from [27]:

$$CCF = \sum_{i,j} \left|u_{\exp}(i,j)\right| \cdot \left|u_{simul}(i,j)\right| \tag{6}$$

where $u_{\exp}(i,j)$ and $u_{simul}(i,j)$ are the normalized experimentally measured field coefficient and the normalized simulation field coefficient on the plane (i,j), respectively. As shown in Fig. 12,

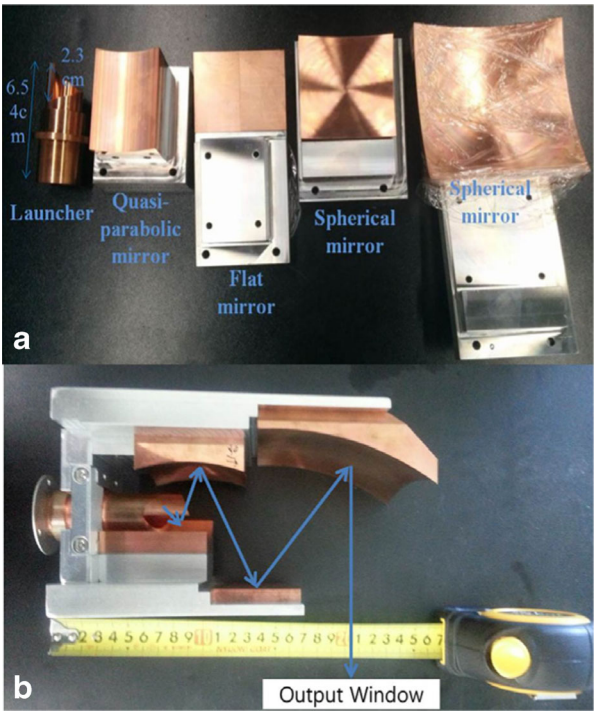

Fig. 11 **a** Fabricated mirrors and the dimpled helical-cut launcher (DHCL). **b** Quasi-optical mode converter (QOMC) assembly (the *blue arrow* indicates the beam path generated from the DHCL, and the *ruler* is in centimeters)

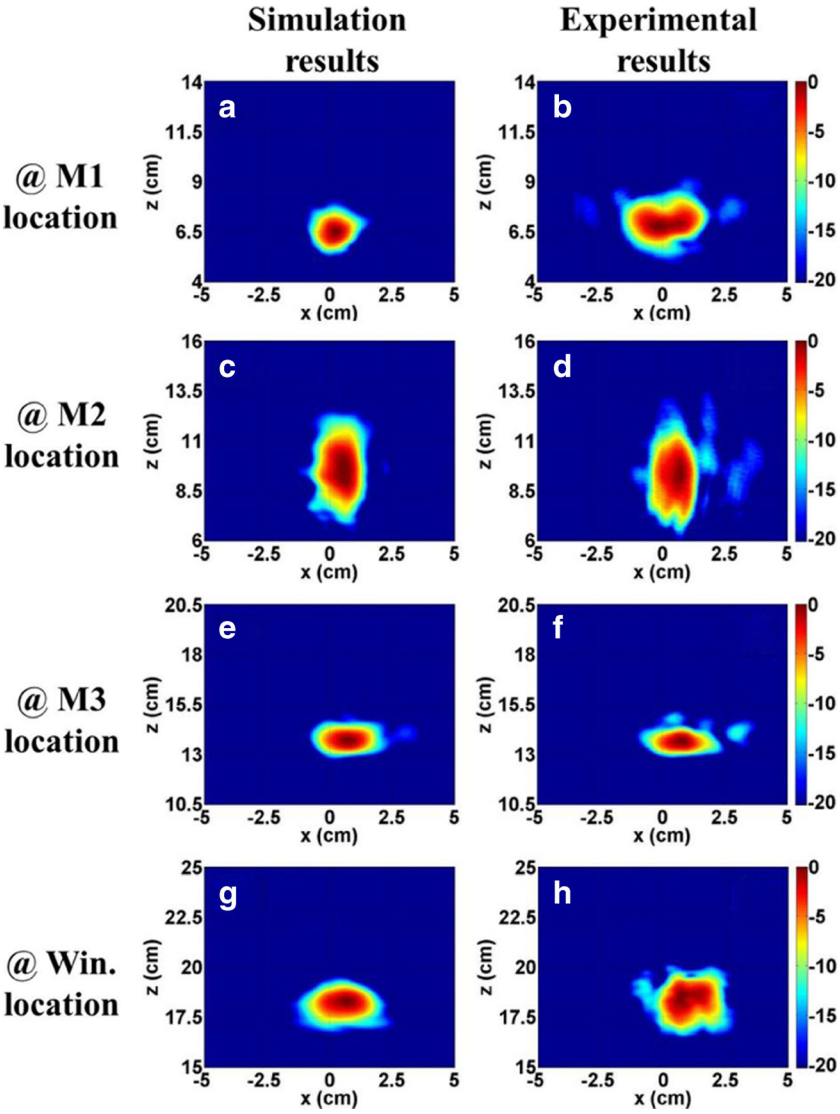

Fig. 12 Electric field intensities as measured by **a**, **c**, **e**, **g** simulation and **b**, **d**, **f**, **h** experiment. The cross-correlation function (CCF) values between **a** and **b**, **c** and **d**, **e** and **f**, and **g** and **h** are 97.6, 97.5, 97.9, and 97.7 %, respectively [25]

the measured beam patterns match the simulation results by more than 95 % at all measurement locations.

2.4 Beam Tunnel, Window, and Transmission Line

A beam tunnel is located between the electron gun and the cavity to prevent propagation of RF to the MIG gun and to avoid generations of unwanted competition modes. As shown in Fig. 13, the beam tunnel has an alternating structure between SiC and Copper rings.

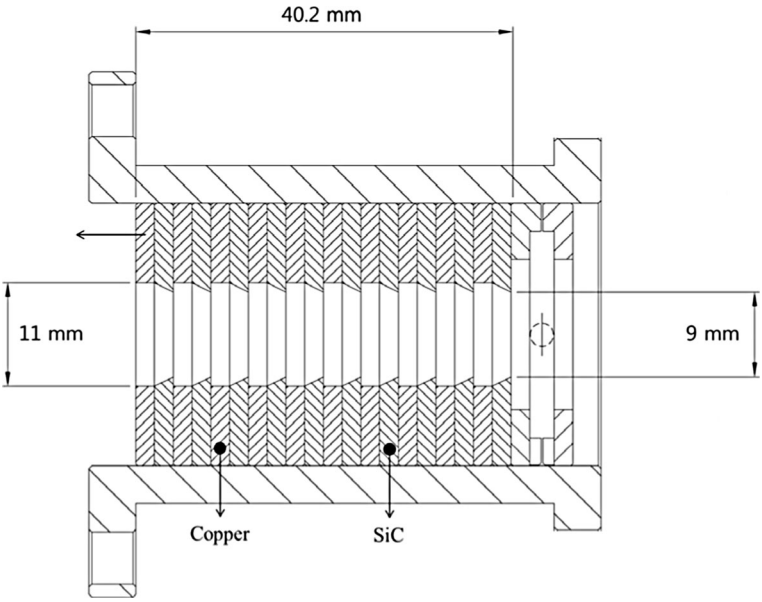

Fig. 13 The geometry of beam tunnel

A fused silica disk (dielectric constant of 3.8 and the loss tangent of 0.0004) was chosen as the output window of the gyrotron. The window thickness was determined to be 5.65 mm to maximize the gyrotron beam transmission with endurance of pressure differences. Figure 14 shows the transmission coefficient comparison between the

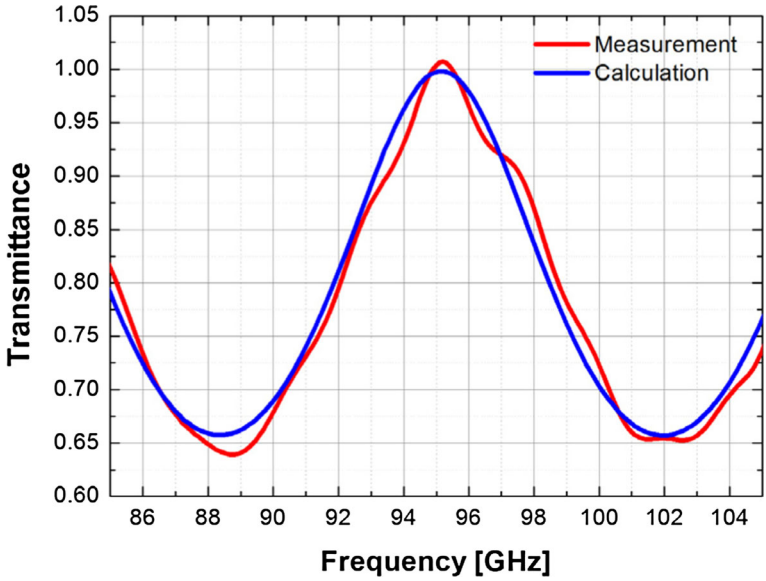

Fig. 14 Comparison of the simulated and experimentally measured transmission through the window

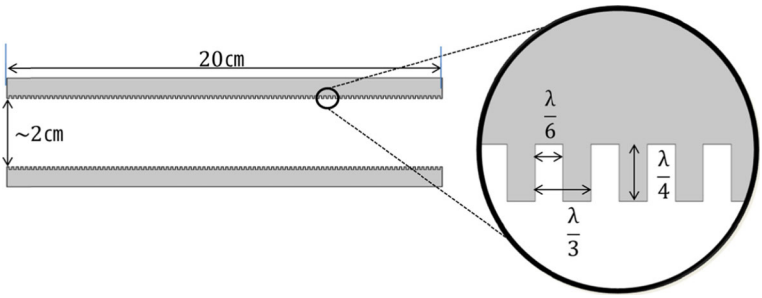

Fig. 15 Corrugated waveguide structure

simulation and the experiment. Some measured data in Fig. 14 possesses unreasonable values of transmittance slightly higher than one, which may come from an incomplete calibration error of the vector network analyzer (VNA) used in the experiment. However, these measurement errors do not affect the result in estimating the transmission value. At the operating frequency, both the simulation and experimental measurement show window loss of less than 1 %. To focus the gyrotron output beam outside the tube, an additional matching optics unit (MOU) consisting of an external spherical mirror was designed and positioned 39 cm from the window. Based on the Gaussian optics equation, the mirror curvatures of the MOU are 19 cm in the *x*-axis and 37 cm in the *z*-axis. The focused beam from the MOU mirror couples to a corrugated waveguide located at a beam waist position, 19 cm from the MOU mirror with a beam waist size of 2 λ. The designed parameters of the corrugated waveguide are shown in Fig. 15. The beam waist size of 2 λ was chosen in order to fit the existing corrugated waveguide. The pitch length, width of corrugation, and corrugation depth are $\lambda/3$, $\lambda/6$, and $\lambda/6$, respectively. Figure 16 shows the results of the Surf3D simulation, in which it is apparent that the gyrotron beam trajectory out of the gyrotron tube coupled well with the corrugated waveguide predicted by the Surf3D simulation.

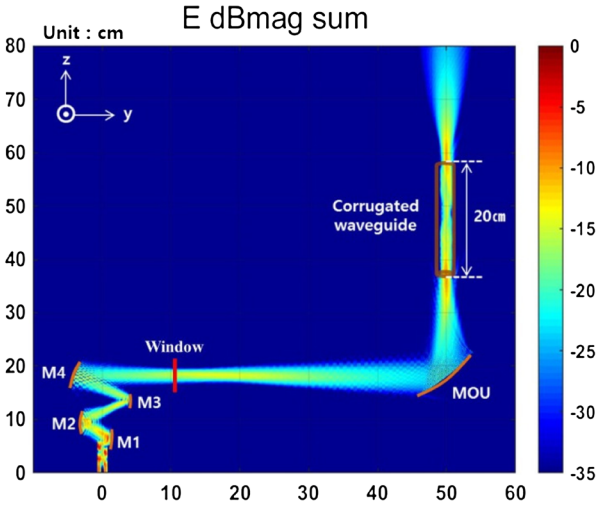

Fig. 16 Output beam path along the propagation direction from QOMC to the corrugated waveguide

3 Experimental Setup and Results

3.1 Experimental Setup

All individual gyrotron components were fabricated and assembled according to the design specifications in Sect. 2. Figure 17 shows the assembled W-band gyrotron inserted in a superconducting magnet. Figure 18 shows the schematic for the gyrotron test setup. The gyrotron received power from a 20-μs pulse modulator capable of 40 kV. A horn antenna collected the output beam signal and transmitted the signal to a heterodyne frequency system constructed at the testing facility to measure the exact frequency.

The output power was measured calorimetrically with a laser power meter (Scientech Model 360401), positioned at the window with an angle of 45° between the surface of the window and the calorimeter to prevent the gyrotron output beam from being reflected back to the system. Carbon paint (Nextel velvet coating 811–21) was added to the surface of the calorimeter to increase the absorption coefficient in the W-band. The output power was also validated with a new power measurement method recently developed in [31].

3.2 Experimental Results

Typical traces for the beam voltage, current, and RF detector signals are shown in Fig. 19. The measured output power and frequency are plotted in Fig. 20 as a function of variations in the primary magnetic field, while the beam voltage and current were maintained to be 40 kV and 7 A, respectively. The primary magnetic field was varied from 3.50 to 3.61 T, and the maximum power of 65 kW was achieved in a magnetic field of 3.52 T. The calorimetric

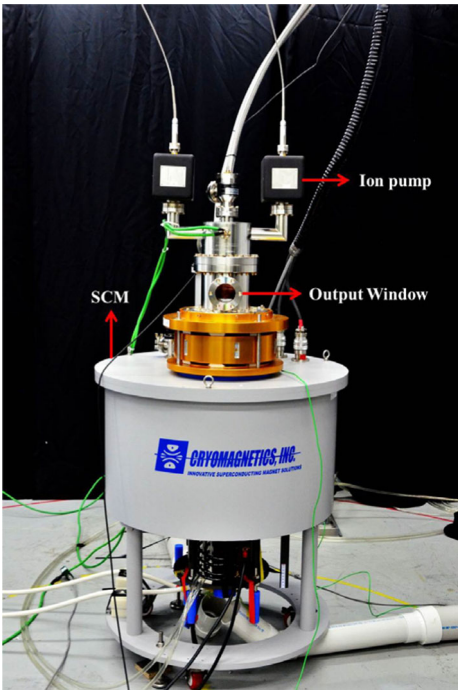

Fig. 17 W-band gyrotron in a superconducting magnet

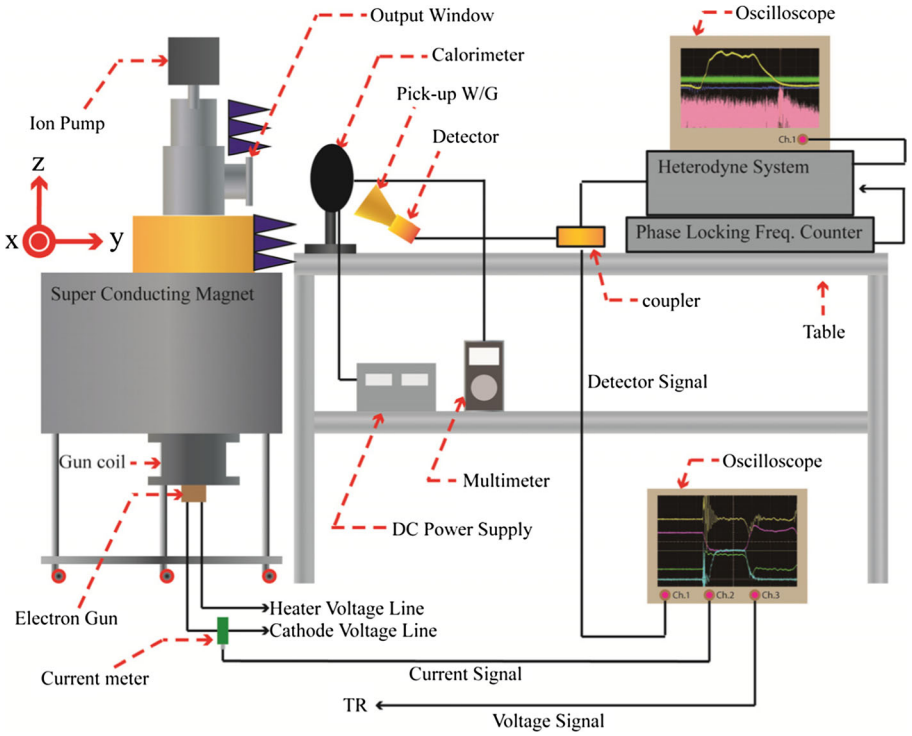

Fig. 18 Schematic of the gyrotron performance test setup

measurement error in power was ±2.5 kW as represented in Fig. 20. The measurement results are compared to the simulation results from MAGIC and UGDT codes. A significant discrepancy between the experiment and the simulation was observed, and detailed analysis was discussed in Sect. 3.4.

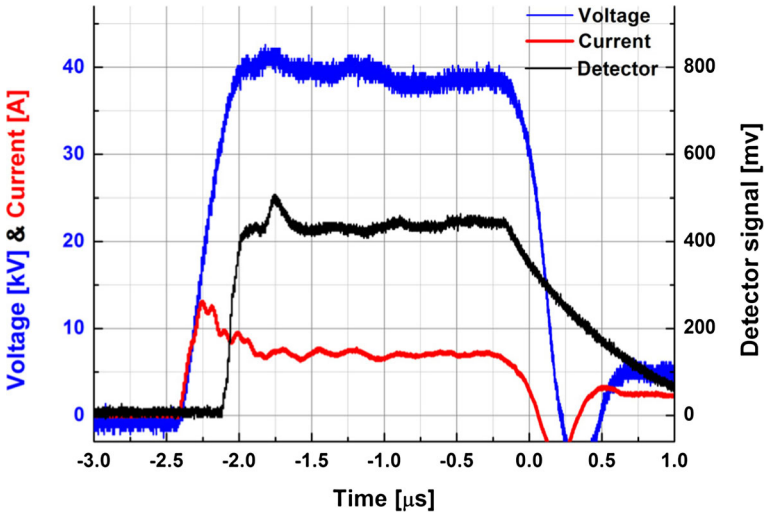

Fig. 19 Measured beam voltage, current, and RF signals

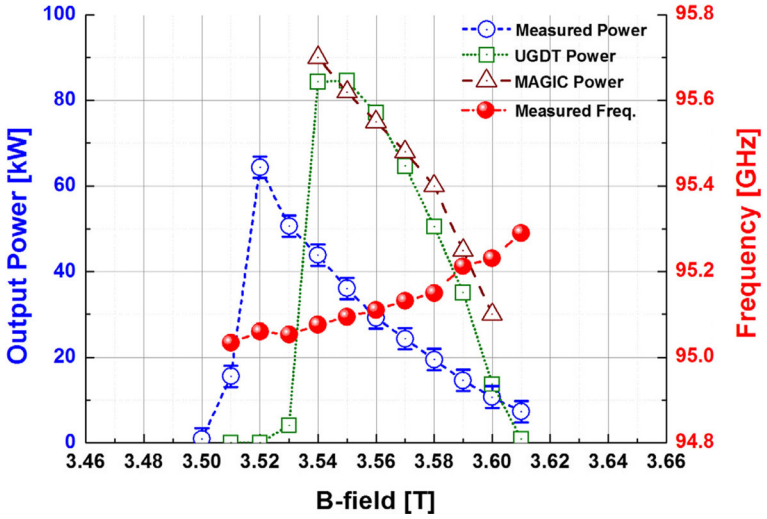

Fig. 20 The comparison between experiment and simulation results on frequency and output power measurements as a function of the primary magnetic field

Figure 21 shows the measured output power as a function of varied cathode voltages between 30 and 42 kV, in a fixed magnetic field of 3.54 T. The output power increases linearly with the cathode voltage, as expected.

3.3 Output Beam Quality

We scanned the output beam pattern to determine whether the beam shape conforms to a Gaussian beam shape and to measure the output beam size. To compare with simulation results

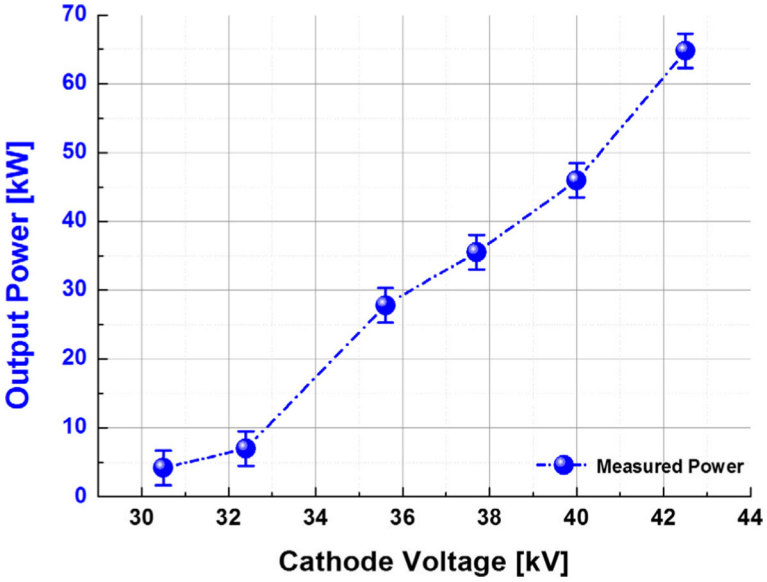

Fig. 21 Measured output power as a function of cathode voltage variation in a magnetic field of 3.54 T

obtained from the Surf3d code and in consideration of the detector linearity and scanning range, the measurement positions were selected to be at 40, 50, and 60 cm from the center of the gyrotron. The calculated beam radius and the experimentally measured beam pattern at these positions are shown in Fig. 22, demonstrating that the measured beam shape is an excellent fit with the Gaussian beam pattern. In Fig. 23, the measured horizontal and vertical beam sizes at different propagation locations are compared to the analytic Gaussian beam

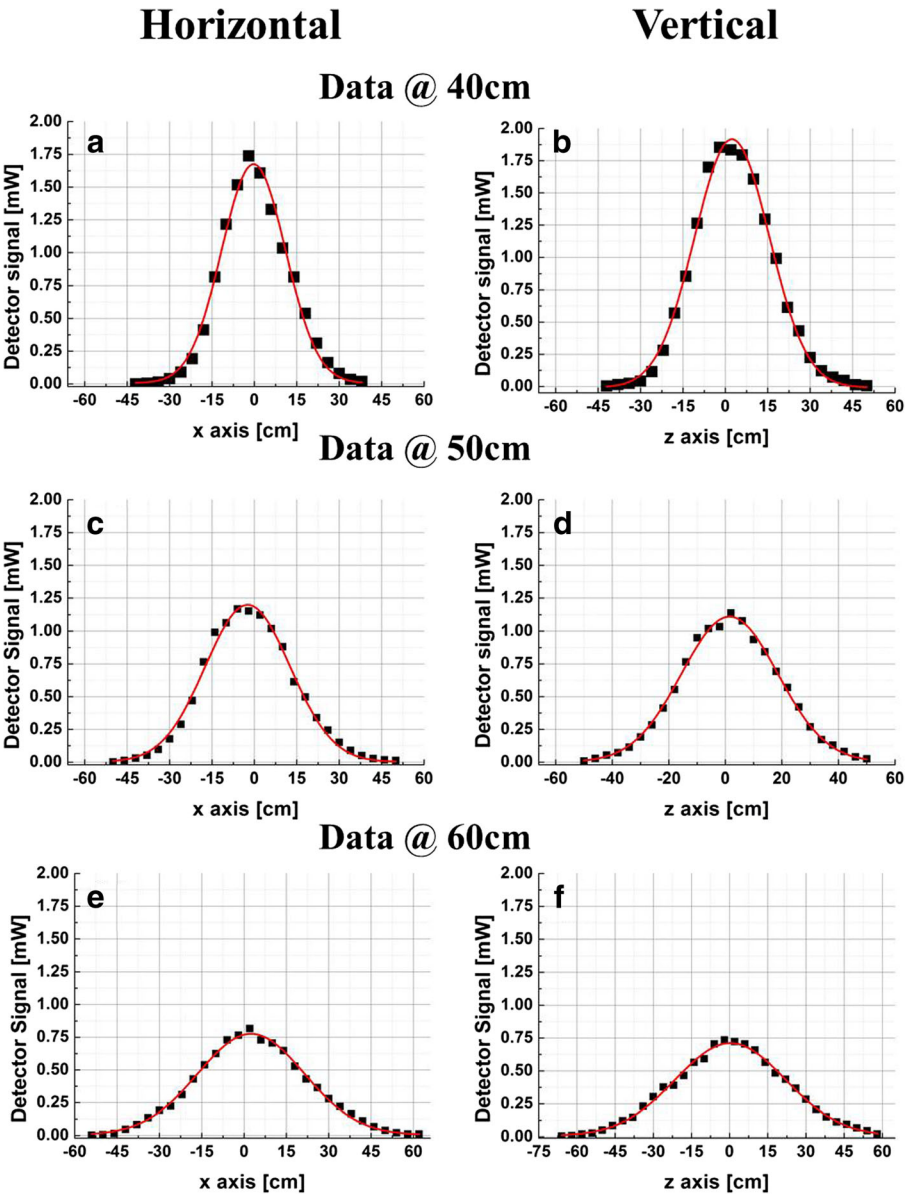

Fig. 22 Measured beam profiles: **a** and **b**, **c** and **d**, and **e** and **f** are the scanning results at 40, 50, and 60 cm, respectively. The *black dots* are the experimental results, and the *red solid lines* show the corresponding Gaussian fitting curves

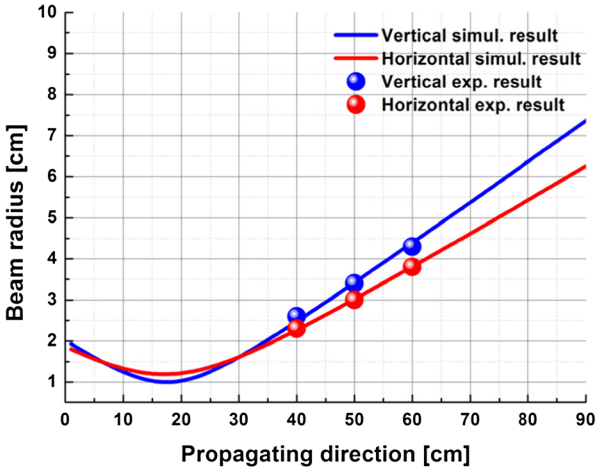

Fig. 23 Measured horizontal and vertical beam sizes (*red* and *blue dots*, respectively) compared to those of the simulated Gaussian horizontal and vertical beam expansions (*red* and *blue curves*, respectively)

expansions with the designed beam waist sizes, and it is apparent that they are in excellent agreement.

The output beam exhibits a slightly elliptical shape, a difference as small as λ at the beam waist location. For this reason, the MOU mirror was positioned to correct the beam shape to the symmetrical Gaussian shape so that the beam would couple with the corrugated waveguide. The output beam patterns at the MOU mirror location and at the end of the corrugated waveguide were made visible using a liquid crystal paper (LCP), as presented in Fig. 24. Figure 24a shows that a qualitatively well-shaped Gaussian beam was achieved, and Fig. 24b shows that this beam was propagated without any mode conversion in the corrugated waveguide.

3.4 Discussions

The gyrotron produced a maximum output power of 65 kW with 23 % efficiency, whereas the MAGIC simulation predicted 90 kW with 32 % efficiency, a difference of approximately 9

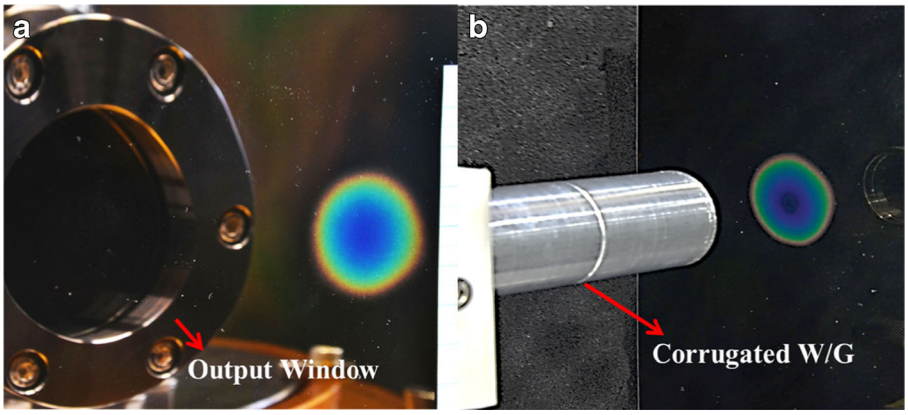

Fig. 24 Photographs of the actual beam pattern on the liquid crystal paper (LCP) measured at **a** the MOU position and **b** after the corrugated waveguide

percentage points between the simulation and experiment. This reduced efficiency in the experiment is thought to be attributed to several reasons: The internal diffraction loss in the QOMC from Surf3D simulation was approximately 8 % in total (from each mirror, around 2 % of incoming power was diffracted). The window dielectric loss was as small as 1 %. Therefore, the total power loss from 90 kW is around 81.9 kW (corresponding efficiency of 29 %), which does not satisfactorily agree to 23 % efficiency measured in experiment. Additional 6 percentage point reduction in efficiency may come from nonuniform electron beam. The simulation was done under the assumption of an ideal electron beam case that does not consider the electron velocity spread, the finite thickness of the beam, the nonuniform emission of the beam, possible tube misalignment, etc. These nonideal parameters affect the gyrotron efficiency in the range of a few percentage points. From all of these effects combined, the simulated maximum efficiency may be reduced by approximately 7–9 percentage points, although clear experimental verification of the efficiency reduction is a quite challenging work that exceeds the scope of this work.

4 Conclusions

The high-power W-band gyrotron has been developed successfully in Korea. Critical components of the gyrotron were designed by internally developed simulation codes, as well as commercially available codes such as CST PS, Surf3D, LOT, and MAGIC. The cavity and mode converter were cold tested and compared to the simulation results, which were thus shown to be in good agreement with each other. The gyrotron components were fabricated and assembled, and the experiment was successfully performed. The gyrotron output power was measured to be 65 kW with 23 % efficiency. The output beam pattern from the window was measured to be in excellent agreement with the simulation, matching the Gaussian curves by more than 95 %. Furthermore, the final coupling to the corrugated waveguide showed excellent results without loss, proving that the final gyrotron beam can be successfully shaped and delivered to the end user. In conclusion, Korea's first gyrotron with a kilowatt power level in the W-band was successfully developed, and its excellent performance characteristics have been demonstrated. More advanced gyrotron code development including electron beam's optical and thermal velocity spread as well as mode competition is as an urgent future plan in Korea which we believe that high frequency, high-power gyrotron research including Korea Fusion Demonstration Reactor (K-DEMO) might become feasible with the accomplishment.

Acknowledgments This work was partially supported by the National Research & Development Program through the National Research Foundation of Korea (NRF) funded by the Ministry of Science, ICT & Future Planning (NRF-2014M1A7A1A03029874) and (NRF-2013R1A1A2061062).

References

1. B. L. Smith, and M. H. Carpentier, The microwave engineering handbook, Chapman & Hall, London, New York, 2003
2. I. Ogawa, K. Yoshisue, H. Ibe, T. Idehara, and K. Kawahata, Long-pulse operation of a submillimeter wave gyrotron and its application to plasma scattering measurement, Rev. Sci. Instrum., 65, 1788–1789, 1994

3. A. Kasugai, R. Minami, K. Takahashi, N. Kobayashi, and K. Sakamoto, Development of a 170GHz high-power and CW gyrotron for fusion application, IRMMW-THz 2005. 30th Int. Conf., 287–288, 2005
4. G. Dammertz, S. Alberti, A. Arnold, E. Borie, V. Erckmann, G. Gantenbein, E. Giguet, R. Heidinger, J. P. Hogge, S. Illy, W. Kasparek, K. Koppenburg, M. Kuntze, H. P. Laqua, G. LeCloarec, Y. Legoff, W. Leohardt, C. Lievin, R. Magne, G. Muller, G. Neffe, B. Piosczyk, M. Schmid, K. Schworer, M. Thumm, and M. Q. Tran, Development of a 140-GHz 1-MW Continuous Wave Gyrotron for the W7-X Stellarator, IEEE Trans. Plasma Sci., 30, 808–818, 2002
5. T. Shimozuma, S. Kubo, M. Sato, H. Idei, Y. Takita, S. Ito, S. Kobayashi, Y. Mizuno, Y. Yoshimura, K. Ohkubo, H. Funaba, S. Inagaki, T. Kobuchi, S. Masuzaki, S. Muto, M. Shoji, H. Suzuki, N. Noda, Y. Nakamura, K. Kawahata, N. Ohyabu, O. Motojima, and LHD Experimental Group, ECH system and its application to long pulse discharge in large helical device, Fusion Eng. Des., 53, 525–536, 2001
6. J. P. Hogge, F. Albajar, S. Alberti, P. Benin, T. Bonicelli, S. Cirant, D. Fasel, T. Goodman, S. Illy, S. Jawla, C. Lievin, I. Pagonakis, A. Perez, B. Piosczyk, L. Porte, T. Rzesnicki, M. Thumm, and M.Q. Tran, The European 2MW, 170GHz Coaxial Cavity Gyrotron for ITER, IRMMW-THz 2007. 32nd Int. Conf., 38–40, 2007
7. T. Rzesnicki, B. Piosczyk, S. Kern, S. Illy, J. Jianbo, A. Samartsev, A. Schlaich, and M. Thumm, 2.2-MW Record Power of the 170-GHz European Preprototype Coaxial-Cavity Gyrotron for ITER, IEEE Trans. Plasma Sci., 38, 1141–1149, 2010
8. K. Sakamoto, A. Kasugai, K. Takahashi, R. Minami, N. Kobayashi, and K. Kajiwara, Achievement of robust high-efficiency 1 MW oscillation in the hard-self-excitation region by a 170 GHz continuous- wave gyrotron, Nature Phys., 3, 411–414, 2007
9. M. Yu. Glyavin, A. G. Luchinin, A. A. Bogdashow, V. N. Manuilov, M. V. Morozkin, Yu. Rodin, G. G. Denisov, D. Kashin, G. Rogers, C. A. Romero-Talamas, R. Pu, A. G. Shkvarunetz, and G. S. Nusinovich, Experimental study of the pulsed terahertz gyrotron with record-breaking power and efficiency parameters, Radiophys. Quantum Electron., 56, 497–507, 2014
10. Y. Yamaguchi, T. Saito, Y. Tatematsu, S. Ikeuchi, V. N. Manuilov, J. Kasa, M. Totera, T. Idehara, S. Kubo, T. Shimozuma, K. Tanaka, and M. Nishiura, High-power pulsed gyrotron for 300 GHz-band collective Thomson scattering diagnostics in the large helical device, Nucl. Fusion 55, 013002, 2015
11. J. H. Booske, R. J. Dobbs, C. D. Joye, C. L. Kora, G. R. Neil, G. S. Park, J. Park, and R. J. Temkin, Vacuum electronic high power terahertz sources, IEEE Trans. THz Sci. Technol., 1, 54–72, 2011
12. L. A. Samoska, An overview of solid-state integrated circuit amplifiers in the submillimeter-wave and THz range, IEEE Trans. THz Sci. Technol., 1, 9–24, 2011
13. M. Thumm, High power gyro-devices for plasma heating and other applications, J. Infrared Milli. Terahertz waves, 26, 483–503, 2005
14. E. A. Nanni, A. B. Barnes, R. G. Griffin, and R. J. Temkin, THz dynamic nuclear polarization NMR, IEEE Trans. THz Sci. Technol., 1, 145–163, 2011
15. C. D. Joye, R. G. Griffin, M. K. Hornstein, K. N. Hu, K. E. Kreischer, M. Rosay, M. A. Shapiro, J. R. Sirigiri, R. J. Temkin, and P. P. Woskov, Operational characteristics of a 14W 140GHz gyrotron for dynamic nuclear polarization, IEEE Trans. Plasma Sci., 34, 518–513, 2006
16. T. Idehara, T. Saito, I. Ogawa, S. Mitsudo, Y. Tatematsu, L. Agusu, H. Mori, and S. Kobayashi, Development of terahertz FU CW gyrotron series for DNP, Appl. Magn. Reson., 34, 265–275, 2008
17. A. C. Torrezan, M. A. Shapiro, J. R. Sirigiri, R. J. Temkin, and R. G. Griffin, Operation of a continuously frequency tunable second harmonic CW 330GHz gyrotron for dynamic nuclear polarization, IEEE Trans. Electron Devices, 58, 2777–2783, 2011
18. M. Pilossof, and M. Einat, Note: A 95GHz mid-power gyrotron for medical applications measurements, Rev. Sci. Instrum., 86, 2015
19. P. P. Woskov, A reflected power isolator for a 10kW, 28GHz gyrotron, IEEE MTT-S, 1–3, 2013
20. T. Idehara, I. Ogawa, S. Mitsudo, M. Pereyaslavets, N. Nishida, and K. Yoshida, Development of frequency tunable, medium power gyrotrons as submillimeter wave radiation sources, IEEE Trans. Plasma Sci., 27, 340–354, 1999
21. P. P. Woskov, H. H. Einstein, and K. D. Oglesby, Application of fusion gyrotrons to enhanced geothermal systems (EGS), Bull. Am. Phys. Soc., 58, 2013
22. P. P. Woskov, H. H. Einstein, and K. D. Oglesby, Penetrating rock with intense millimeter waves, IRMMW-THz 2014. 39th Int. Conf., 1–2, 2014
23. P. P. Woskov, and P. Michael, Millimeter wave heating, radiometry, and calorimetry of granite rock to vaporization, J. Infrared Milli. Terahertz waves, 33, 82–95, 2012
24. F. Paul, W. Menesklou, G. Link, X. Zhou, J. Hauselt, and J. R. Binder, Impact of microwave sintering on dielectric properties of screen printed Ba0.6Sr0.4TiO3 thick films, Jour. Eur. Ceram. Soc., 34, 687–694, 2014
25. M. V. Kartikeyan, E. Borie, and M. Thumm, Gyrotrons high power microwave and millimeter wave technology, Springer, Berlin, Germany, 2004

26. E. Borie, and O. Dumbrajs, Calculation of eigenmodes of tapered gyrotron resonators, Int. J. Electronics, 60, 143–154, 1986
27. A. Sawant, S. G. Kim, M.C. Lin, J.H. Kim, Y. J. Hong, J. So, E. M. Choi, Validation of 3-D time domain particle-in-cell simulations for cold testing a W-band gyrotron cavity, IEEE Trans. Plasma Sci., 42, 3989–3995, 2014
28. Surf3d computational Ver. 2.43, GUI Ver. 1.21 user manual, Lexam research. www.calcreek.com
29. D. S. Tax, E. M. Choi, I. Mastovsky, J. M. Neilson, M. A. Shapiro, J. R. Sirigiri, R. J. Temkin, and A. C. Torrezan, Experimental results on a 1.5 MW, 110 GHz gyrotron with a smooth mirror mode converter, J. Infrared Mill. Terahz Waves, 32, 358–370, 2011
30. S. G. Kim, D. S. Kim, M. S. Choe, W. Lee, J. So, and E. M. Choi, Cold testing of quasi-optical mode converters using a generator for non-rotating high-order gyrotron modes, Rev. Sci. Instrum., 85, 2014
31. S. G. Kim, J. H. Kim, D. S. Kim, W. Lee, J. H. Won, W. Jang, and E. M. Choi, A real-time, direct power measurement of a high power electron cyclotron maser using a simple one-point Schottky detector signal, IEEE Trans. THz. Sci. Tech., 5, 779–785, 2015